Pyrolyzed Ca-impregnated lignite for aqueous phosphate removal: Batch and column studies

Hasara Samaraweera [a,*], John Edwards [b], Claudia Reid [b], S. Sameera Perera [c], Rooban Venkatesh K.G. Thirumalai [d], Charles U. Pittman Jr. [a], Todd Mlsna [a]

[a] Department of Chemistry, Mississippi State University, MS, USA
[b] Department of Mechanical Engineering, Mississippi State University, MS, USA
[c] Lumigen Instrument Center, Wayne State University, Detroit, MI 48201, USA
[d] Institute for Imaging & Analytical Technologies, Mississippi State University, Starkville, MS 39762, USA

ARTICLE INFO

ABSTRACT

Lignite is an abundant carbon material with a variable surface structure and low cation density The introduction of metal (hydr)oxide phases has improved the anionic binding potential of lignite. In this study, activated lignite (A−L), Ca^{2+}−modified lignite (Ca−L), and Ca^{2+}−modified activated lignite (Ca−A−L) were synthesized to remove aqueous phosphate. Lignite was first activated (KOH: lignite, mass ratio, 3:1) at 750 °C to prepare A−L, improving its surface area by ~984-fold. Ca−L (27 wt% Ca) showed a large phosphate uptake (227.3 mg/g) (adsorbent dose 50 mg, 25 mL of 10–1500 ppm phosphate, 24 h, 25 °C, initial pH 6), due to the large amounts of micro-sized $CaCO_3$, $Ca(OH)_2$, and CaO particles in Ca−L. These particles actively precipitate phosphate/hydrophosphate as $CaHPO_4/Ca_3(PO_4)_2$. The breakthrough capacity of a 2.0 g Ca−L bed column (bed height 2.5 cm, diameter 1 cm) was 58.2 mg/g (flow rate 1.5 mL/min, 25 °C, initial $[PO_4^{3-}]$ = 46.6 mg/L, particle size, 125–150 μm), ~4 fold lower than the maximum Langmuir sorption capacity. An interference study indicated that Ca−L is highly selective for phosphate. Spent Ca−L may improve soil fertility as it retains more phosphate species for later slow-release to the soil. Unit weight of phosphate can be removed by Ca−L more inexpensively than Norit ROW and Darco KB (two commercial activated carbon carbons). Precipitated Ca^{2+} phosphates/hydrophosphates in exhausted Ca−L can be recovered using HCl and Ca−L recycled. Moreover, low-cost lignite is a promising carbon support for the future synthesis of different value-added products.

1. Introduction

Water quality degradation resulting from eutrophication is a global environmental and economic problem. High phosphorus concentration is an obstacle in effluent desalination [30]. When the phosphorus concentration in water exceeds 100 μg/L [15], harmful algal blooms occur. The USEPA recommends limiting the orthophosphate (bioavailable form of P) levels below 10 μg/L in water bodies. Point (e.g., sewage effluent) and non-point (e.g., agricultural run-off) sources contribute to eutrophication. Phosphate can be removed via biological (using microbes, microalgae, and halophytes), physical (size exclusion, membrane filtration, and adsorption), and chemical (precipitation, flocculation, and coagulation) methods. Each suffers from different pitfalls like membrane fouling, unrecoverable precipitates, and large space needs. Adsorption is a simple way to reduce pollutant levels in complex environmental matrices.

Lignite is abundant in many countries, and was utilized in environmental remediation [11–13,33]. Cation-deficient lignite achieved a poor (0.19 mg/g) phosphate removal at an 5 mg/L initial phosphate concentration and pH 2.3 [25]. Therefore, the carbonaceous surfaces should be modified with cations. Recent anionic adsorptive remediation has included a La-modified granular ceramic (H. [49]), a mesoporous silica and ligand embedded composite [2], an Al-modified biochar [51], bifunctional nanocomposites (W. [50]), UiO-66 nanocomposites (W. [50]), MgO-modified biochars [34,47], dolomite-modified biochar [16], magnesium oxide nanoflake-modified diatomite adsorbents [48], and a $Mg(OH)_2/ZrO_2$ composite [18]. The K_{sp} values of metal-phosphate complexes determine their phosphate removal performance. Ca^{2+} and Fe^{2+}/Fe^{3+} have low pK_{sp} values with phosphates and demonstrated high phosphate removal efficiencies. A well-dispersed nano-CaO on

Ca^{2+}-modified sludge carbon (CaCO$_3$/sludge = 1:2) removed 117 mg/g aqueous phosphate via hydroxylapatite formation (pK$_{sp}$ = 53.28 at 25 ºC) [14,58].

This study describes the preparation of three lignite-based materials for phosphate mitigation. Ca^{2+}−modified lignite (Ca−L) exhibited a high phosphate uptake (227.3 mg/g at 25 ºC), due to its high Ca content (27 wt% Ca). Activated lignite (A−L) is highly porous (S$_{BET}$ = 2854 m^2/g) and having a higher phosphate removal ability than lignite (8.0 mg/g vs 5.2 mg/g). A−L was used to introduce a greater amount of Ca^{2+}, followed by calcination at 800 ºC, which generates Ca^{2+}−modified activated lignite (Ca−A−L). But, Ca−A−L had only a 1 wt% C (bulk C), therefore, its adsorption behavior was not further investigated. Sorption isotherms were conducted at optimized pH values (pH 5.5, 5, and 6 for lignite, A−L, and Ca−L) and an environmentally relevant pH value (pH = 7). The column performance, synthetically polluted real wastewater, and interference studies were performed. Phosphate (per gram) removal cost in Ca−L is 3 times less than lignite. Owing to high phosphate uptake, easy regeneration using HCl, high phosphate selectivity, and 100% phosphate removal from simulated wastewater, Ca−L has more practical importance than other sorbents in the study. Spent Ca−L after heavy phosphate loading can be used as a potential slow-release fertilizer.

2. Materials and methods

2.1. Materials

Lignite (~100 g) from Mississippi Lignite Mining Company, Ackerman, MS, USA was washed, oven-dried (1 atm, air, 100 ºC, 48 h), ground for 2 min (high-speed multifunctional grinder, 36,000 revolutions/min, model no: HC150T2) and sieved (150–300 μm). XRD data shows the presence of graphitic carbon (2θ = 24.8º and 34.4º) in lignite (Fig. 2A) in agreement with our previous studies [35]. Further, this lignite has a high SiO$_2$ content (~19.9%). Analytical grade (Sigma Aldrich) calcium hydroxide, ferric chloride, ferrous sulfate heptahydrate, sodium hydroxide, concentrated sulfuric acid, ammonium molybdate, and ascorbic acid were purchased and used.

2.2. Preparation of activated - lignite (A−L)

KOH-activated lignite was produced as per [22]. Lignite (10 g) was mixed with an aqueous KOH solution (30 g in 50 mL), (3:1, mass ratio) in a 250 mL Erlenmeyer flask and vigorously stirred for 1½ h at 65 ºC. This mixture (90 g) was kept in a ceramic crucible and oven-dried (1 atm) at 105 ºC overnight. This mixture was carbonized in a muffle furnace under N$_2$. Pyrolysis employed a 50 °C/min ramp rate to 750 °C, followed by holding at 750 °C 1 h. After cooling, (27.1 g) (67.8% yield) of solid crude A−L was obtained. Preliminary pyrolyzes were performed at 650, 750, and 850 °C. Pyrolysis at 750 ºC produced the maximum activated carbon surface area and was chosen as the optimum production temperature of this synthesis. This KOH modified lignite (A−L) (27.1 g), was neutralized with aqueous 37% wt. HCl (50 mL, once), followed by washing with DI water (~1500 mL) and oven-drying (105 ºC, overnight) to give a 2.2 g (22% yield based on starting lignite) of A−L.

2.3. Production of Ca^{2+}−modified lignite (Ca−L) and Ca^{2+}−modified activated lignite

Calcium-modified lignite (Ca−L) was prepared using conventional wet impregnation. Ca(OH)$_2$ (10.0 g) was added into DI water (50 mL). Pre-dried raw lignite (10.0 g) was added into this viscous solution, then this solution was stirred overnight, and oven-dried (105 ºC, 1 atm) for 24 h. After drying, a weight of 19.2 g was obtained. This solid was carbonized in a muffle furnace under N$_2$. Pyrolysis employed a 20 °C/min ramp rate to 800 °C, followed by holding at 800 °C for 2 h. This heat

treatment resulted in Ca(OH)$_2$, CaO, and CaCO$_3$ phases on the surface. After cooling, a 15.8 g (79% yield based on both Ca(OH)$_2$ and lignite) of Ca−L was obtained. The resulting solid (Ca−L) was washed with ~1000 mL of DI water (pH 7). The adsorbent washing was required to remove residual 3.7 g of Ca^{2+} oxides/hydroxides loosely attached to the lignite [56]. Water washing caused a non-avoidable dissolution of surface Ca^{2+} oxide/hydroxide, and possibly some carbonate into the washing waters (Fig. 3C). This washed product was oven-dried (105 ºC, 48 h) before doing any adsorption experiments, producing a weight of 12.1 g (C yield, 35.4% yield based on starting lignite). Calcium-modified activated lignite (Ca−A−L) was prepared using the same synthesis conditions, but starting with activated lignite, instead of lignite. Ca−A−L has almost no remining carbon (< 1%), after the two calcination steps used; to pyrolyze A−L at 750 ºC and then to carbonize at 800 ºC after treating with Ca^{2+}. Further characterization and sorption behavior of Ca−A−L was not assessed.

2.4. Material characterization

Detailed characterization methods are provided in the Supporting Information. The pH values of NaCl solutions (25 mL in each) were adjusted using 1 M NaOH and 1 M HCl to determine the adsorbents' point of zero charge. Scanning electron microscopy employed a JEOL JSM-6500F FE-SEM operated at 5 kV. EDS spectroscopy was performed on a Zeiss, EVO 40 scanning electron microscope with a BRUKER EDX system. C, H, and N bulk elemental analyses were performed using an ECS 4010 elemental combustion system (Costect Analytical Technologies Inc.). Powder X-ray diffraction patterns recorded on a Rigaku ultima III instrument (Cu-K$_\alpha$ (λ = 1.54 nm)) and crystallographic structures in adsorbents were identified before and after PO$_4^{3-}$ sorption. Functional groups or elemental oxidation states on pre- and post-PO$_4^{3-}$ sorbed surfaces were determined using X-ray photoelectron spectroscopy (Thermo Scientific K-Alpha XPS system). The complete acid digestion of Ca−L (1 g) was performed to determine its Ca content.

2.5. Adsorption experiments

Adsorptions were investigated using the batch experiments conducted in a Thermo Forma Orbital Shaker (200 rpm, 25 ± 0.5 °C) run 24 h at varied pH levels. Unless otherwise specified, 0.05 of the adsorbents and 50 ppm phosphate (25 mL) were used in each experiment. Adsorption experiments were conducted in triplicate. The effect of pH on phosphate adsorption was conducted under environmentally relevant pH conditions (i.e., pH = 5.0–9.0). A 24 h kinetic study was conducted, removing the samples at pre-determined times (from 5 min to 24 h). Phosphate-laden adsorbents were filtered using 11 μm filter paper and preserved for later analysis. Phosphate sorption on filter papers was negligible. Adsorption isotherm experiments were conducted by varying the phosphate concentrations from 25 to 1500 ppm at 25, 35, and 45 °C.

Phosphate concentrations in the filtrates were acquired by a Shimadzu UV-2550 double beam spectrophotometer at 830 nm using the ascorbic acid method [21]. Batch sorption data were analyzed using Excel and Origin 2020 software (detailed data evaluation methods and equations are presented in Section 2.3 in Supporting Information). The phosphate ion adsorption capacities (q$_e$) were determined as:

$$q_e = \frac{Ci - Ce}{m} \quad V$$

Removal efficiency (R%) was calculated as

$$R\% = \frac{Ci - Ce}{Ci} \times 100\%$$

Here, C_i = initial liquid-phase phosphate adsorbate concentration (mg L^{-1}), C_e = equilibrium liquid-phase phosphate adsorbate concentration (mg L^{-1}); V = volume of phosphate solution (L); m = mass of adsorbent used (g).

2.6. Fixed-bed column experiments

The fixed-bed column study was conducted with Ca−L using a C-18 empty cartridge (BOND Elut., internal diameter of 1 cm) as the column. The column was packed with 2.00 g of the Ca−L (particle size 125–150 μm), generating an adsorbent bed height of 2.5 cm between two supporting layers of glass wool (occupied bed volume, 2 cm^3 and un-occupied bed volume = 2 mL). An aqueous solution of phosphate (total volume, ~3.3 L, influent phosphate concentration, 46.6 mg/L, pH 7, and 25 °C) was pumped from bottom to top of the column using a single StEP™ pump (w/o fittings) equipped with an average flow of 1.5 mL/min.

The Ca−L bed allowed for a constant non-zero permeability at room temperature (25 ºC). Effluent samples were collected at regular time intervals (7.5 mL in each 5 min) to determine the phosphate concentration. The effluent flow was continued until there was no further adsorption. The breakthrough curve was expressed as C_i/C_o as a function of effluent time/volume for a given bed height [5].

3. Results and discussion

3.1. Elemental analysis and physicochemical properties

A−L has a lower carbon percentage than lignite (39.4% vs. 15.2%) and produced a higher H/C ratio (Table 1). This denotes that A−L is less aromatic than lignite. However, the H/C ratio of Ca−L is lower than raw lignite (Table 1), indicating that the carbon aromaticity of Ca−L was increased upon Ca^{2+} addition and pyrolysis. A low carbonaceous phase (~11.5%) remained in Ca−L after pyrolysis of Ca(OH)$_2$-lignite 1:1 mixture. Much of the starting carbon was mineralized to form CaCO$_3$ (14.0%) at 800 ºC and some of the SiO$_2$ content formed CaSiO$_3$ (40.6%). Ca−L reported a ~99% ash content (Table 1). However, this value is higher than the ash contents obtained by bulk (76.8%) and TGA (71.8%) analyses (Fig. 1A). Al$_2$O$_3$ (2.0%) and SiO$_2$ (25.7%) quantified in A−L contributed to a higher ash content (36.4%) than in lignite (25.0%) (Table 1). High moisture content in A−L (11.4%) attributes to the deliquescence of metallic K.
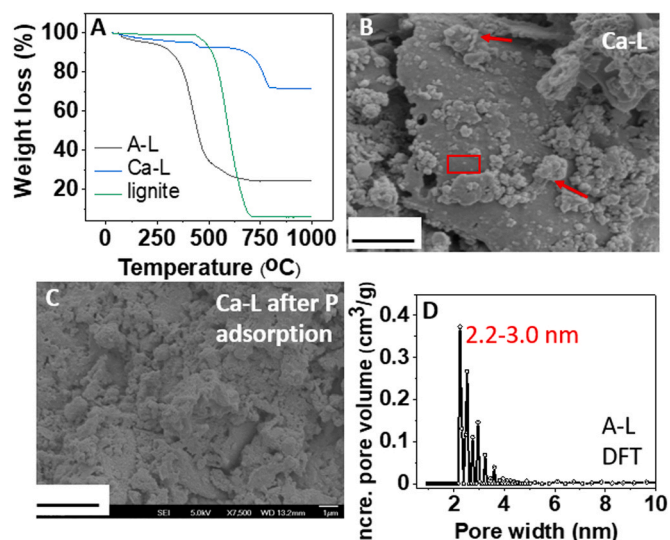

Fig. 1. A) TGA analysis of lignite, A−L, and Ca−L SEM images of Ca−L before (B) and after (C) P uptake (scale bar 1 μm). In (A), the red square showed CaSiO$_3$, Ca(OH)$_2$, CaO, and CaCO$_3$ primary particles (crystal sizes were ~10.2 nm, ~28.4 nm, ~18.6 nm, and ~20 nm, respectively) deposited on Ca−L, whereas red arrows denote particle clusters (< 2 μm) formed due to Ca (OH)$_2$ modification to the surface. (D) DFT- pore size distributions of A−L.

A−L is highly porous as seen in Fig. S1C. SEM analysis of Ca−L depicted nano-sized CaSiO$_3$, Ca(OH)$_2$, CaO, and CaCO$_3$ primary particles (20–25 nm) and micro-sized (1–2.5 μm) aggregates on the surface (Fig. 1B). These aggregates are formed during the adsorbent production at 800 ºC. After phosphate sorption, smoother A−L and Ca−L surfaces were detected, which was due to either phosphate adsorption or leaching/precipitation (Fig. 1C).

SEM-EDX analyses of pre- and post-P uptake adsorbent samples provided the surface elemental distribution [38] to a depth of 3.1 μm. Atomic percentages of Si (10.5%), O (30.0%), K (0.6%), Ca (0.2%), and

Table 1
Physical properties of lignite, A−L, and Ca−L.

Parameter		Lignite-based adsorbent		
		Lignite	A−L	Ca−L
BET (m^2/g)		2.9 ± 0.1	2854.0 ± 5.0	18.0 ± 0.3
Average pore volume (cm^3/g)		0.0008	0.5	0.005
Average pore size (Å)		12.1	7.0	10.0
Micropore volume (cm^3/g)		0.0003	0.43	0.0034
Moisture (%)		3.2	11.4	1.7
C%	Combustion analysis	39.4	15.2	11.5
H%		2.7	2.4	0.5
N%		1.2	1.0	0.8
H/C		0.8	1.9	0.5
Ca%		1.3	0	5.6
Mg%[a]	AAS	0.3	0.5	0.0
K%		0.1	0.3	0.15
Fe%		0.0	0.55	0.62
Si%		9.3	12.0	9.8
Al%		0.3	0.5	1.8
Ash (%)	Proximate analysis	25.0	36.4	99.0
PZC		3.9	6.5	13.0
Yield (%)[b]		N/A	22.0	60.5

[a]Mg content of Ca−L was below under the detection limits of AAS. [b]Yield is based on the original weight of raw lignite (washed + dried) used.

Table 2

Elemental distribution of adsorbents estimated using SEM-EDX elemental mapping (Only the prominent elements are presented here).

Adsorbent	Atomic percentages							
	C	O	Ca	K	Fe	Al	Si	P
Before P adsorption								
Lignite	73.4	13.2	0.01	0.01	–	–	0.06	0.4
A−L	54.4	26.6	0.04	0.6	–	–	12.2	0.6
Ca−L	27.7	52.9	15.3	0.07	–	–	1.1	2.2
After P adsorption								
Lignite	66.5	24.1	0.8	0.2	–	–	4.5	0.8
A−L	54.6	24.4	0.03	0.2	–	–	20.1	0.4
Ca−L	9.2	56.7	14.0	0.2	–	–	7.6	5.9

C (35.6%) were found on the A−L surface before P uptake (Table 2). Ca is evenly and densely distributed on the Ca−L surface (Fig. S1M) before P uptake. After phosphate sorption, the P peak is absent in the P-laden A−L EDX spectrum (Fig. S2L) due to the low EDX P signal-to-noise ratio, resulting from a low density of surface P adsorption. P peak is visible in the Ca−L EDX spectrum after P uptake (P-laden S2N). After Ca−L contact with a pH 6 phosphate solution, its SEM-EDX spectrum lost a portion of its Ca (from 15.3% to 14.0%), indicating Ca^{2+} leaching (Table 2). Ca^{2+} leaching from Ca−L generates a higher Ca^{2+} solution concentration near the surface, where $Ca_3(PO_4)_2/Ca(HPO_4$ precipitate. After P sorption, the equilibrium solution pH was ~13 (Fig. 3B), in agreement with the precipitation of $Ca_3(PO_4)_2/Ca(HPO_4$ ($K_{sp} = 2.1 \times 10^{-33}$, 1.3×10^{-7}) back onto the Ca−L surface.

3.2. Surface area

BET surface area of A−L (2854 ± 5.0 m^2/g) was higher than raw lignite (2.9 ± 0.1 m^2/g) (Table 1). A−L has the highest surface area reported for any lignite-based adsorbent [3,37,40]. Demineralization by KOH, followed by pyrolysis at 750 ºC (50 ºC/min heating rate, 1 h) resulted in a formation of a porous material [39]. KOH activation begins at 700 ºC and is complete at ~750 ºC [19,27,29]. Its pore volume was also larger than the feed lignite (0.43 vs. 0.0003 cm^3/g) (Table 1). Metallic K diffuses to the carbon crystalline layers and expands them. These metallic species can be removed after acid rinsing, which improves the surface area. To generate metallic K, temperatures above 700 ºC are required [19,22]. Three activation temperatures (650 ºC, 750 ºC, and 850 ºC) were initially used to experimentally determine the optimum (750 ºC) for A−L production. Temperature increment from 650 to 750 ºC increased surface area from 499 to 2854 m^2/g, but decreased (2242 m^2/g) at 850 ºC; due to the lignite sintering, which shrinks char particles and realigns the carbon backbone [13]. N_2 adsorption-desorption isotherms of lignite, A−L, and Ca−L exhibit type I adsorption behavior as the pores were saturated by N_2 within $P/P_o < 0.2$ (Fig. S4A−C) indicating well defined microporous structure; micropores are filled at low pressures. Typically activated carbons contain both micropores and mesopores [8].

A high KOH: lignite (3:1) mass ratio caused a low A−L product yield (22.0%) (Table 1), in agreement with previous reports [8]. The resulting A−L has only 15.2% C, a 91.6% drop in carbon content compared to raw lignite (39.4% C). KOH-guided activation generates more microporosity, while NaOH produces more mesoporosity [9,20]. In comparison to previously reported activated carbons [7], A−L displays a DFT pore size distribution with wider pore diameters (2.2–2.5 nm) (Fig. 1D). [17] observed the formation of pores with wider pore diameters with the increase of KOH: carbon mass ratio in activated carbons. In contrast, decreasing the KOH: carbon ratio produces activated carbons with narrow pore sizes (~0.55 nm) [43]. Moreover, DFT analysis revealed the existence of large mesopore (~10–20 nm) fractions in lignite and Ca−L (Fig. S4D and F). However, a substantial amount of small mesopores (2.2–2.5 nm) in A−L accounts for its higher surface area (2854 m^2/g) than lignite and Ca−L (2.9 m^2/g and 18.0 m^2/g).

Ca−L had a surface area (18.0 ± 0.3 m^2/g) six times greater than the raw lignite (Table 1) due to $CaCO_3$, $Ca(OH)_2$, and CaO particle formation in it. Hydrated phosphate anions have diameters of 0.339 nm [57], which is smaller than lignite, A−L, and Ca−L pore sizes (Table 1), therefore, they all have access to hydrated phosphate.

However, A−L's very high surface area did not lead to high phosphate removal (3.0 mg/g at 50 ppm initial PO_4^{3-} concentration) (Table 3). In the same PO_4^{3-} concentration, Ca−L (18.0 ± 0.3 m^2/g) has a 28-times greater phosphate uptake, 227.3 mg/g than A−L. This is due to large amounts of $Ca(OH)_2$, $CaCO_3$, and CaO particles formed in the Ca−L, which provide leached Ca^{2+} ions, precipitating $CaHPO_4$ and $Ca_3(PO_4)_2$ onto the surface.

3.3. XRD analysis

The lignite XRD pattern displayed two peaks at $2\theta = 24.8º$ (0 0 2) and 38.4º (1 0 0) (Fig. 2A) due to the graphitic carbon existence [55]. The peak at $2\theta = 26.6º$ (SiO_2) is hidden within the broad graphitic region. The broad peak of $2\theta = 22.7º$ in the A−L XRD spectrum (Fig. 2B) is assigned to amorphous graphitic carbon resulting from lignite's pyrolysis [59]. High-temperature activation (750 ºC, 1 h) degrades organic carbon in lignite in the presence of excess KOH, leading to more disorder and loss of carbon. The crystalline peak at $2\theta = 26.6º$ (SiO_2) (JCPDS No. 76–1390) was invisible as it was hidden in the broad graphitic peak region.

After pyrolysis at 800 °C, the Ca−L XRD spectrum exhibited several intense and narrow peaks (Fig. 2C), indicating the formation of crystalline compounds. Two peaks at $2\theta = 26.6º$ and 29.5º (Table S5) belong to $CaSiO_3$ and $CaCO_3$ [28], with average crystal sizes, 10.2 nm and ~19.7 nm (these sizes were calculated according to Scherrer formula, assuming that the samples are free of strain) (Supporting Information). The peaks centered at 2θ values of 17.8º, 33.9º, 47.6º, and 50.1º in Ca−L can be attributed to $Ca(OH)_2$ (Fig. 2C). A trace of CaO ($2\theta = 32.1º$ and 36.3º) was also found. Typically, pyrolysis temperatures > 800 °C are required to generate CaO crystals from $CaCO_3$ [6]. These crystals are nano sized ($Ca(OH)_2$, ~28.4 nm, and CaO, ~18.6 nm). After P uptake, $CaHPO_4$ phases at $2\theta = 20.9º$, 29.3º, 35.9º, and 48º (JCPDS No. 9–348) [23] and $Ca_3(PO_4)_2$ at $2\theta = 29º$, 39º, and 43º [10,24,32] were identified (Fig. 2D). The average $CaHPO_4$ and $Ca_3(PO_4)_2$ sizes were 32.5 nm and 33.5 nm.

3.4. Effect of pH and Ca^{2+} leaching test

A pH vs. phosphate uptake study was conducted from pH 5–9 (Fig. 3). The predominant phosphorus species that exist in the pH range of 0–4.7 are H_3PO_4 and H_2PO_4, from 4.7 to 9.7 H_2PO_4 and HPO_4^{2-}, and

Table 3

Langmuir adsorption isotherm parameters for lignite, A−L, and Ca−L at 25, 35 and 45 °C (adsorbent dose 50 mg, 25 mL of 10–1500 ppm phosphate concentration, 24 h, at pH values (5.5, 5, and 6 for lignite, A−L, and Ca−L, respectively)[a].

Temperature	pH	Adsorbent	q_m (mg/g)[b]	K_L	R^2
25 ºC	5.5	lignite	5.2	0.015	0.99
	5	A−L	8.0	0.060	0.99
	6	Ca−L[c]	227.3	0.005	0.99
35 ºC	5.5	lignite	14.0	0.008	0.99
	5	A−L	24.6	0.020	0.99
	6	Ca−L[c]	250.0	0.050	0.99
45 ºC	5.5	lignite	35.0	0.003	0.99
	5	A−L	59.1	0.001	0.99
	6	Ca−L[c]	384.6	0.020	0.99

[a] The non-linear isotherm forms were used here to calculate the respective parameters.

[b] Maximum Langmuir adsorption capacity (mg/g).

[c] Ca−L is not a true adsorbent. It's a stoichiometric reagent, that can release Ca^{2+} to precipitate phosphate as $CaHPO_4/Ca_3(PO_4)_2$.
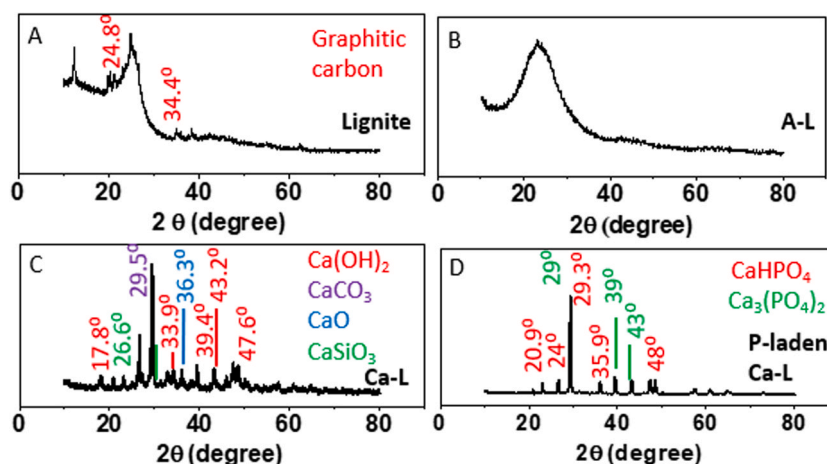
Fig. 2. XRD analysis (A) lignite, (B) A−L, (C) Ca−L before, and (D) P-laden Ca−L after P uptake.
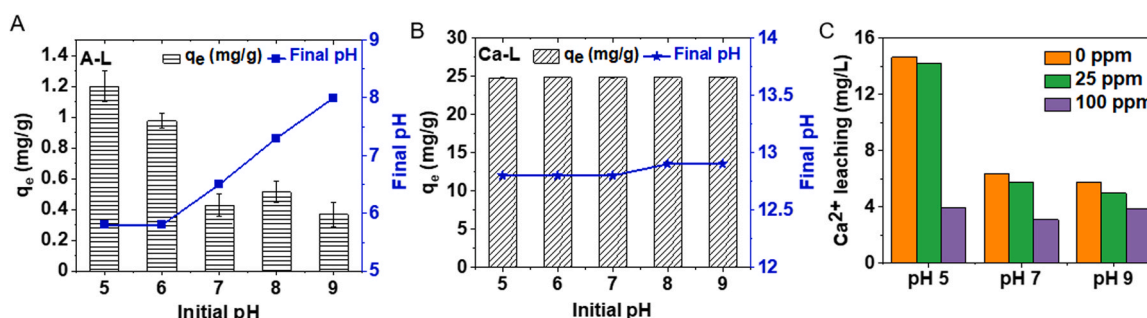

Fig. 3. pH dependence for phosphate sorption for (A) A−L and (B) Ca−L over the pH range from pH 5–9 (adsorbent dose 50 mg, 25 mL of 50 ppm phosphate concentration, 24 h, 25 ℃). (C) calcium leaching test for Ca−L (0–100 ppm phosphate concentrations and pH values of 5, 7, and 9, 25 ℃, 24 h).

from 9.7 to 14.0 HPO_4^{2-} and PO_4^{3-}. A−L's phosphate sorption dropped upon increasing the pH from 5 to 9 (Fig. 3A) as it is negatively charged above pH 6 (PZCs ≈ 6.5–6.7), which repels H_2PO_4 and HPO_4^{2-}. A−L has a phosphate uptake (1.2 mg/g) at pH 5, which dropped to 0.14 mg/g at pH 9. After phosphate-binding, the equilibrium pH increased slightly from pH 5 but slightly decreased (6−8) for initial pH values from 6 to 9.

Ca−L's P uptake has little pH dependence (24.8 mg/g from pH 5–9) (Fig. 3B). The equilibrium pH after phosphate uptake was constant (~13) for all pH levels tested because hydroxide ions were released from the surface or leached as $Ca(OH)_2$ during calcium phosphate and hydrophosphate formation (Section 3.7). Similar hydroxide/phosphate exchange occurred with a $La(OH)_3$-modified sorbent and equilibrium pH increases after sorption occurred at initial pH values 3–6 [54]. The basic final pH in Ca−L, resulting from $Ca_3(PO_4)_2$/$CaHPO_4$ precipitation, can be utilized for treating acidic water discharging from various industries (e.g., wine and beer) [31]. The use of Ca−L (PZC~13) as a soil conditioner could be beneficial in reducing soil pH fluctuations, improving microbial degradation [46].

Ca^{2+} leaching (14.6 ppm) from Ca−L is greatest at pH 5 in a phosphate-free solution (Fig. 3C). More $Ca(OH)_2$ and $CaCO_3$ were identified on the initial Ca−L surface, in which $Ca(OH)_2$ is far more soluble ($K_{sp} = 5.5 \times 10^{-6}$, at pH 7) than $CaCO_3$ ($K_{sp} = 2.9 \times 10^{-9}$). When the phosphate solution concentration increased to 100 ppm, the amount of Ca^{2+} remaining in the solution after leaching decreased significantly to less (3.9 ppm), as the released Ca^{2+} was fixed on the surface as $Ca_3(PO_4)_2$ ($K_{sp} = 2.1 \times 10^{-33}$) and $CaHPO_4$ ($K_{sp} = 1.3 \times 10^{-7}$). Antunes et al. [1] reported that brushite (CaH PO_4·$2H_2O$) precipitated at the initial pH = 2, and a high leached Ca^{2+} concentration (Ca^{2+}-biochar made by 20% $Ca(OH)_2$ wt. only gave brushite). Similar surface amounts of Ca^{2+} oxides/hydroxides/carbonates were dissolved in water at pH 7.

3.5. Adsorption kinetics and isotherm studies

The pseudo-second-order kinetic model data better fit all three (R^2 values from 0.97 to 0.99) than the first-order model (R^2 values from 0.72 to 0.97) (Table S2). Ca−L achieved uptake equilibrium after 4 h ($k_2 = 0.17$ min^{-1}), which is faster than $Ca(OH)_2$-treated natural clinoptilolite [26]. Phosphate-binding onto highly porous A−L ($t_{eq} = 1.5$–2 h) occurred faster than the phosphate uptake by Ca−L.

Both Langmuir and Freundlich isotherm models (Tables 3 and S2) describe the phosphate removal by lignite, A−L, and Ca−L well. Modification of lignite with $Ca(OH)_2$ increased the affinity for PO_4^{3-} by ~30 fold at pH 6 (Table S2). A−L shows a slightly higher K_f value than lignite and is bound to slightly more PO_4^{3-} ions. Adsorption intensity (1/n) (Table S2) denotes the type of adsorption (irreversible, favorable, and, unfavorable). The phosphate uptakes by all three adsorbents are favorable (1/n < 1) at 25 ℃.

Maximum Langmuir adsorption capacities were A−L (8.0 mg/g) and Ca−L (227.3 mg/g) versus lignite (5.2 mg/g) at their optimum pH levels of 5, pH 6, and 5.5, respectively (Table 3). The sorption capacities at 45 ℃ were A−L (59.1 mg/g) and Ca−L (384.6 mg/g) versus lignite (35.0 mg/g). Ca−L has the highest Langmuir k_L value (0.02 L/mg). However, Ca−L is operating by a stoichiometric precipitation process, so the phosphate high affinity meaning of k_L should not be confused with sorption affinity.

The Ca−L's uptake capacity (~ 227.3 mg/g at both pH 6 and 7 at 25 ℃) is higher than that of our previously developed magnesium and calcium-doped lignite (24.9 mg/g at pH 2.2 at 25 ℃, 15.5 mg/g at pH 7 at 25 ℃) [35]. We gained a 10-fold enhancement in phosphate uptake using a higher Ca^{2+} loading on Ca−L than in Ca-Mg lignite (Ca: lignite mass ratio, 1:1 vs 1:10) [35]. Sorption isotherm maximum capacities obtained at pH 7 and 25 ℃ for lignite (1.5 mg/g), and A−L (2.9 mg/g)

were lower than the corresponding capacities obtained at their optimum pH levels, whereas that for Ca−L was unchanged (227.3 mg/g). Ca−L retained more phosphate and will be studied as a material used to improve soil fertility.

3.6. Thermodynamics of phosphate sorption

Negative ΔG values from 25 to 45 °C for lignite (-19.8 to -42.0 kJ/mol), A−L (-18.3 to -27.3 kJ/mol), and Ca−L (-21.8 to -26.8 kJ/mol) (Table S3) indicate that all sorptions are spontaneous, in line with the previously prepared iron oxide adsorbents [52]. Lignite phosphate binding is endothermic ($\Delta H = 303.9$ kJ/mol). When the temperature increased from 25 to 45 °C, phosphate sorption capacity rose (from 5.2 mg/g to 35.0 mg/g for lignite) (Table 3) and the sorption occurs by chemisorption (ΔH, 20–400 kJ/mol). A−L and Ca−L phosphate uptakes are exothermic ($\Delta H = -160.4$ and -37.7 kJ/mol) and the physisorption can play a role in phosphate uptake. The positive entropy change value for lignite's phosphate removal ($\Delta S = 1.1$ kJ/mol) denotes the increase in the randomness. A−L and Ca−L have negative ΔS values (-444.2 and -41.3 kJ/mol, respectively), illustrating overall order increases in these processes.

3.7. XPS studies and phosphate-binding interactions

C, O, and Si dominate in lignite, A−L, and Ca−L surface regions according to low-resolution (LR) XPS survey spectra, whereas Ca, Al, Fe, Na, and Mg are also present before any phosphate removal occurs (Table S6). LR XPS found C (43.0%), O (40.8%), Al (5.3%), and Si (8.7%) atomic percentages are present on lignite's surface. Ca−L made after impregnating lignite in the Ca^{2+} solution and pyrolyzing at 800 °C, lost to ~70.1% of its precursor lignite's carbon. However, Ca−L surfaces contain $CaCO_3$, accounting for some of the 25.7% atomic percentage of C in its LR XPS. Ca−L's higher surface Ca content vs lignite (9.6% vs. 0%) led to its far higher phosphate uptake.

The HR C1s XPS spectra of all three adsorbents were deconvoluted into five peaks, including C−C/C−H, C−O, C=O, COOR, and CO_3^{2-} (Fig. S7 and Table S7). The Ca−L surface has a higher CO_3^{2-} percentage than lignite (4.2% vs. 3.0%) because of $CaCO_3$ formation on Ca−L during 800 °C pyrolysis. The surface of Ca−L is positively charged (PZC~13) at its optimal pH (= 6) and attracts HPO_4^{2-}/PO_4^{3-} anions (Fig. 3B). Therefore, the electrostatic interaction plays an initial role in Ca−L's phosphate removal. However, at this pH, Ca^{2+} is released from surface $Ca(OH)_2$ and $CaCO_3$, reacts with phosphate anions, and reprecipitate as $Ca_3(PO_4)_2/CaHPO_4$ particles on the surface. HR C1s XPS analysis depicted a loss in CO_3^{2-} percentage (from 4.2% to 1.7%) and ^-OH percentage (from 7.9% to 6.4%) (Table S7), suggesting a Ca^{2+} leaching from $CaCO_3$ and $Ca(OH)_2$ on the Ca−L surface. These $Ca_3(PO_4)_2/CaHPO_4$ precipitates coincided with an increased solution final pH after phosphate sorption to 13 (Fig. 3B).

In high resolution Ca−L O1s XPS spectra, peaks were assigned at 530.0 eV (M-O), 530.6 eV (M-OH), 531.4 eV (C-O), 532.6 eV (C=O), and 533.7 (COOR) (Table S8 and Fig. 4C). The surface O percentage in Ca−L HR O1s XPS spectrum rose ~6-fold to 61.5 at% vs. lignite due to deposition and formation of CaO, $Ca(OH)_2$, and $CaCO_3$ and other ash-forming minerals like SiO_2 (Fig. 4A and C). After phosphate uptake, the surface ^-OH content dropped on P-laden Ca−L (from 13.8% to 10.9%) (Table S9 and Fig. 4C and F) as Ca^{2+} enters the solution from Ca $(OH)_2$ and HPO_4/PO_4^{3-} salts of Ca^{2+} form. Surface precipitation of $Ca_3(PO_4)_2$, $CaHPO_4$ is more favored, and phosphate is removed by forming water-insoluble Ca^{2+} salts.

The Ca2p HR XPS analysis of Ca−L exhibited a high $CaCO_3$ percentage (8.4%) and small quantities of $Ca(OH)_2$ (1.3%) and CaO ($2p_{1/2}$) (2.4%) (Table S9). CaO will rapidly and exothermically is converted into $Ca(OH)_2$ in water [4]. Ca2p HR XPS P-laden Ca−L spectrum has three peaks, including 347.2 eV ($Ca_3(PO_4)_2$ ($2p_{3/2}$)), 347.8 eV ($CaHPO_4$ ($2p_{3/2}$)), and 348.9 eV ($Ca_3(PO_4)_2$ and $CaHPO_4$ ($2p_{1/2}$)) peaks overlap (Table S9 and Fig. 4G). Stable $CaHPO_4$ (347.8 eV) forms the highest fraction (7.2 at%) of any species resulting from P uptake by Ca−L. A lower intensity (2.2%) peak at 347.2 eV was from $Ca_3(PO_4)_2$ precipitation. Precipitation of $Ca_3(PO_4)_2$ /$CaHPO_4$ from the near-surface region of Ca−L led to a higher surface P atomic percentage (6.9%) after P uptake versus that of lignite (0.2%) (Fig. 4H and Table S10).

According to EDX/XRD/XPS analyses and data obtained from the pH and leaching experiments, phosphate uptake by Ca−L predominantly occurs via the formation of insoluble $Ca_3(PO_4)_2$ and $CaHPO_4$, after the reaction of phosphate species with released Ca^{2+} from the surface (Eqs. (1) and (2)).

$$Ca^{2+} + PO_4^{3-} \rightarrow Ca_3(PO_4)_2 \tag{1}$$

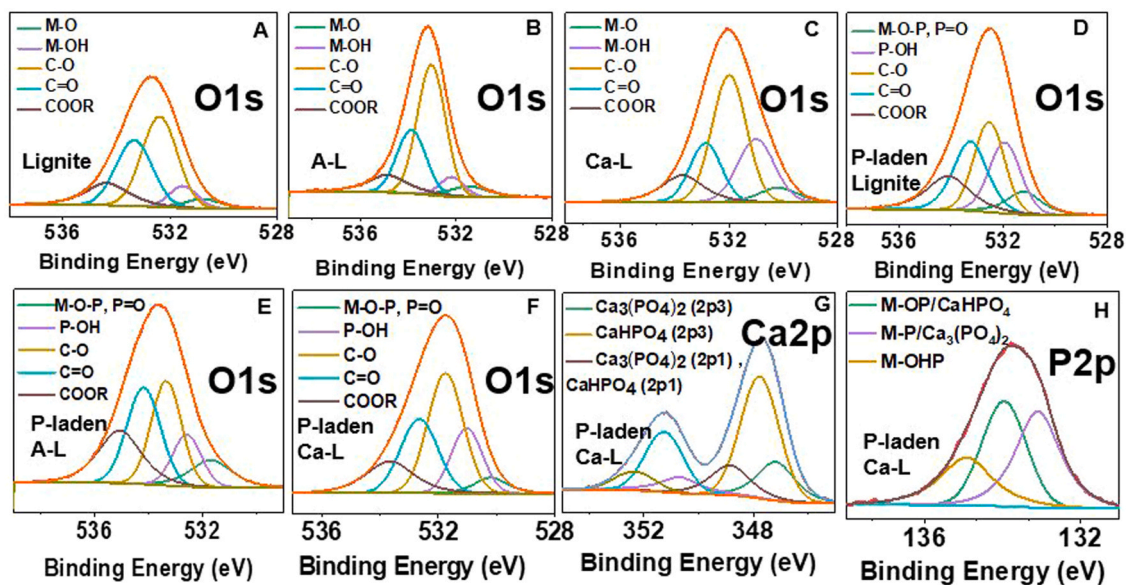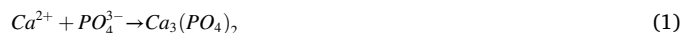$$Ca^{2+} \quad + HPO_4^{2-} \rightarrow CaHPO_4 \tag{2}$$

Fig. 4. HR O1s XPS spectra of lignite, A−L, and Ca−L before P sorption (A-C) versus after P sorption (D-F) at pH values for lignite (5.5), A−L (5), and Ca−L (6). (G) HR Ca2p XPS spectrum for P-laden Ca−L. (H) HR P2p XPS spectrum for P-laden Ca−L.

3.8. Column studies

Fixed-bed column studies provide initial flow information for practical scaling. Fixed-bed column (diameter = 1 cm, particle size, 125–150 μm, 25 ºC) studies were conducted on lignite (3.5 cm bed depth) and Ca−L (2.5 cm and 2.0 cm depths) at a flow rate of 1.5 mL/min for 46.6 mg/L phosphate concentration. The columns were operated under up-flow conditions [44,53]. The process parameters are tabulated in Table 4. Fig. 5A and B present the lignite and Ca−L column breakthrough curves for phosphate sorption. Two major inflection points occur in the breakthrough curves, (1) where the column starts to become saturated (breakthrough point) and (2) where it became saturated (exhaustion point) [36]. Breakthrough points occurred after ~15 h for Ca−L and ~2 min for lignite. The adsorbent surface areas, inherent kinetics, capacities, flow rates, temperatures, particle sizes, and shapes play important roles in the breakthrough time. Lignite has lower phosphate adsorption due to lower BET surface area (2.9 ± 0.1 m^2/g) than Ca−L (18.0 ± 0.3 m^2/g) (Table 1) and reached saturation rapidly. The column uptake capacities were 58.2 mg/g for Ca−L and 4.0 mg/g for lignite (Table 4). Ca−L's column capacity was 4-times lower than its maximum Langmuir phosphate uptake capacity (227.3 mg/g) at 25 ºC (Table 3). In contrast, lignite's column capacity was only 1.3 times lower than that of lignite at 25 ºC (5.2 mg/g).

The effect of bed height (2.5 cm and 2.0 cm) was tested for Ca−L's phosphate uptake. Phosphate breakthrough point occurred within 10 h for a 2.0 cm bed height, reducing the column capacity ~3 fold (18.6 mg/g vs. 58.2 mg/g, for bed heights 2.0 cm and 2.5 cm). Insufficient residence time caused by a lower bed depth led to less time for Ca^{2+} dissolution and precipitation Ca$_3$(PO$_4$)$_2$/CaHPO$_4$. Further studies of larger columns with larger adsorbent particle sizes to aid flow considerations are required to better optimize the column parameters for Ca−L and to achieve a breakthrough uptake closer to its Langmuir capacity. Ca−L's experimental data and the relationship between operating parameters were analyzed using Thomas, Yoon-Nelson, and Adams-Bohart models (Supporting Information). Thomas and Yoon-Nelson models gave better fits to the Ca−L phosphate uptake (Table S11). The Thomas model predicted a Ca−L (2.5 cm bed height) phosphate capacity of 44.6 mg/g vs the observed capacity (58.2 mg/g).

3.9. Ca−L regeneration, selectivity, and real wastewater study

The regeneration of spent Ca−L (Fig. 5C) was examined after phosphate uptake using 20 ppm initial phosphate concentration (0.6 g adsorbent dose, 300 mL solution volume, 24 h, at pH 7 and 25 ºC). Phosphate uptake was 10 mg/g at 25 ºC and pH 7. Stripping employed 0.5 M NaHCO$_3$ (pH = 8.5), 1 M NaOH (pH = 14.8), and 0.5 M HCl (pH = 0.2). Desorption capacities were calculated by multiplying the desorbed concentration (C_{des}) by the stripping agent volume (V) and

dividing it by the adsorbent weight (m). Desorbability (%) was defined as the ratio of desorbed capacity vs adsorbed capacity. HCl stripping gave the highest desorption with the stripping strength order HCl (76.7%) > NaHCO$_3$ (42.9%) > NaOH (0.4%). About 76% of precipitated phosphate desorbed in HCl because Ca-phosphates/hydrophosphates are highly soluble in HCl. The low brushite (CaHPO$_4$2H$_2$O) solubility in NaOH caused poor phosphate desorption (0.4%) with 1 M NaOH.

The competitive ion (SO$_4^{2-}$, NO$_3^-$, HCO$_3^-$ and Cl$^-$) effect on phosphate uptake by Ca−L was tested using binary systems at different competitive ion concentrations (0.05 and 0.5 mol/L) (Fig. 5D). Different solution volumes of competitive ions were added to 25 mL of 50 mg/L phosphate solution. Ca−L is highly selective for phosphate anion uptake when SO$_4^{2-}$, NO$_3^-$, HCO$_3^-$, and Cl$^-$ are present. Acid−base properties, geometric shapes, and metal complexing abilities determine the selectivity of an adsorbent for phosphate [45]. According to the hard/soft acid-base theory, Ca^{2+} in Ca−L is a hard acid, and electron pair donating ability is highest in PO$_4^{2-}$ and decreases according to the order of PO$_4^{2-}$ > HCO$_3^-$ > SO$_4^{2-}$ > Cl$^-$ > NO$_3^-$. A maximum phosphate capacity of 24.8 mg/g was obtained at all three concentrations (0.05 M and 0.5 M) for all four competitions.

Ca−L showed a 10 mg/g phosphate uptake (100% removal) from 20 mg/L phosphate spiked real wastewater (Fig. 5E). Ca−L is a better candidate to treat real wastewater as it reduces phosphate below the USEPA's suggested aqueous phosphate level (0.01 ppm) to avoid eutrophication [41].

3.10. Economic significance

The current study demonstrated that Ca−L was effective in precipitating aqueous phosphates/hydrophosphates as Ca$_3$(PO$_4$)$_2$/CaHPO$_4$. Fig. 5F displays the cost comparison for unit weight of the adsorbent, including lignite, A−L, Ca−L, Ca−A−L, and two commercial activated carbons, Darco KB and Norit ROW GAC. The total cost of an adsorbent includes the cost for source/chemicals, energy, and labor [15]. The lignite is affordable (0.02$/kg) however, the energy is required for its preparation (drying and milling of lignite during its cleaning), raising its total cost ($7.9/kg of lignite). Although the production cost of Ca−L is higher than lignite (due to required CaCO$_3$), its phosphate (per gram) removal is ~ 26% that of lignite; Ca−L has a higher phosphate-binding potential than lignite, reducing the ratio (cost $/weight of PO$_4^{3-}$). The high cost of KOH ($47.6/kg) and the high KOH: lignite mass ratio (3:1) account for the large cost of A−L ($24.6/g of PO$_4^{3-}$). Two commercial activated carbons, Darco KB ($244/kg) and Norit ROW GAC ($103/kg) have low phosphate removal potentials (6.5 mg/g and 8.9 mg/g) [42] resulted in large costs (90 and 30 times higher than Ca−L) to remove 1 g of PO$_4^{3-}$.

Basic Ca−L can restore acidic soils and increases soil fertility. Due to its high phosphate uptake, Ca−L could potentially serve as a slow-release phosphate fertilizer. It removes 100% phosphate from spiked-real wastewater. Also, ~76% adsorbed phosphate in Ca−L can be desorbed after 1st cycle of acidic regeneration. Moreover, Ca is non-toxic and abundant, favoring real applications. Overall, our results indicated that Ca−L is a better candidate for phosphate removal with a low phosphate stripping cost. However, further tests are required to evaluate its use for industrial applications. This study includes one regeneration step for Ca−L; further regeneration steps are needed to assess its full reusability potential. Ca^{2+} compounds initially present on Ca−L supply the Ca^{2+} for phosphate precipitation. Thus, larger initial loadings might last through more cycles but not be as efficient in total phosphate uptake per initial Ca content. This study can be further enhanced by employing other Ca additives such as CaCl$_2$, CaCO$_3$ etc. Preparation of Ca−A−L requires more energy expenditure than Ca−L since its production involves two pyrolysis steps. Also, a huge carbon loss occurred during that process.

Table 4
Column parameters for phosphate uptake by Ca−L vs. lignite.

| Parameter	Ca−L	Lignite
Bed depth (cm)	2.5	3.5
Bed volume (cm^3)	2.0	2.7
Weight of carbon (g)	2.0	1.4
Flow rate (mL/min)	1.5	1.5
EBCT (Empty Bed Contact Time)	1.3	1.8
Column capacity (mg/g)	58.2	4.0
Breakpoint capacity (mg/g)	19.5	0.3
Initial PO$_4^{3-}$ concentration (mL/min)	46.6	46.6
PO$_4^{3-}$ concentration at exhaustion point/C_x (mg/L)	44.7	45.0
PO$_4^{3-}$ concentration at break point/C_b (mg/L)	5.4	2.3
Exhaustion volume/V_x (L)	3.3	0.3
Break point volume/V_b (L)	0.9	0.0075
Total time to reach exhaustion point/T_x (min)	3000	60
Total time to reach break point/T_b (min)	878	2
% saturation	75.6%	18.7%
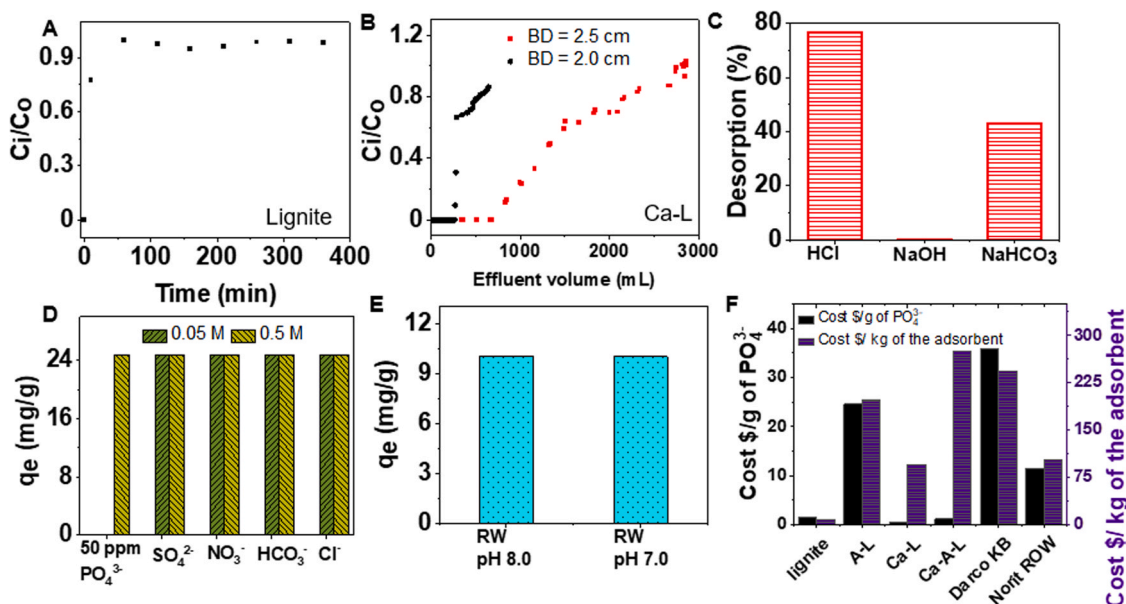
Fig. 5. (A) PO_4^{3-} breakthrough curves of a 46.6 mg/L $[PO_4^{3-}]$ for lignite (bed height = 3.5 cm, diameter = 1 cm, 1.4 g of lignite, particle size 125–150 μm), (B) effect of Ca−L bed heights (2.5 cm vs 2.0 cm) for diameter = 1 cm, 2 g vs. 0.9 g of Ca−L, particle size 125–150 μm. (C) desorption study for Ca−L using HCl, NaOH, and NaHCO$_3$ stripping agents (~25 mL). (D) Effect of competitive ions (0.05 M and 0.5 M) on phosphate sorption by Ca−L (50 ppm PO_4^{3-} concentration, 25 mL solution volume, 25 ℃, 24 h). (E) Ca−L real wastewater phosphate (20 mg/L) uptake study at pH 8.0 and 7.0 (adsorbent dose, 0.05 g, solution volume, 25 mL, 25 ℃, 24 h). Effluent P concentration was below the limit of detection of UV. (F) The cost analysis of lignite, A−L, Ca−L, Ca−A−L, and two commercial activated carbons (Darco KB and Norit ROW GAC). Cost to remove per gram of PO_4^{3-} (Right, Y-axis) and total cost to prepare 1 kg of adsorbent (Left, Y-axis) indicated in the graph.

4. Conclusions

Engineered lignite carbons including, activated lignite (A−L), Ca^{2+}−modified lignite (Ca−L), and Ca^{2+}−modified activated lignite (Ca−A−L) were prepared using an affordable lignite system to mitigate phosphate from aqueous solutions. Although A−L has a very high surface area (2854 m^2/g) and a large pore volume (0.5 cm^3/g), it had poor phosphate sorption capacity. Low surface area Ca−L (18.0 ± 0.3 m^2/g) achieved an exceptional phosphate uptake (384.6 mg/g at 45 ℃), noted to be the highest value among calcium-modified lignite adsorbents. This uptake was due to the substantial amounts of micro-sized CaCO$_3$, CaO, and Ca(OH)$_2$ particles which act stoichiometrically. XRD, EDX, and XPS revealed that these particles release Ca^{2+} precipitating phosphate/ hydrophosphate onto the surface. Spent Ca−L can be recycled effectively using HCl. Furthermore, it exhibited high selectivity towards phosphates and remediates phosphates from synthetically polluted (phosphate spiked) real wastewater. Ca−L shows a high affinity for phosphates in the presence of other anionic contaminants including SO$_4^{2-}$, NO$_3^-$, HCO$_3^-$ and Cl$^-$. Preliminary Ca−L column studies showed the column capacity was 4-times lower than its Langmuir capacity. Therefore, further column studies will be required to determine optimal conditions for adsorption with Ca−L during practical scale-up. Unit weight of phosphate removal cost is less using Ca−L than commercial activated carbons and lignite. High Ca−L phosphate uptake suggests that it could serve as a slow-release phosphate fertilizer. Therefore, studies of the applicability of Ca−L as a soil amendment and its potential commercialization are already planned in a funded study. Moreover, additional interference experiments need to be performed to determine the selectivity of Ca−L for phosphate removal from a variety of real wastewater samples.

Funding

CRediT authorship contribution statement

Hasara Samaraweera: Writing − original draft preparation, Investigation, Methodology. **John Edwards:** Research support. **Charles U. Pittman**: Conceptualization, Writing − review & editing. **S. Sameera Perera**: Data curation, Software, Editing. **Rooban Venkatesh K. G. Thirumalai:** Data curation, Software. **Claudia Reid:** Research support. **Todd Mlsna:** Conceptualization, Supervision, Project administration.

Declaration of Competing Interest

The authors declare that they have no known competing financial interests or personal relationships that could have appeared to influence the work reported in this paper.

Acknowledgments

Appendix A. Supporting information

Supplementary data associated with this article can be found in the online version at doi:10.1016/j.jece.2021.106077.

References

[1] E. Antunes, M.V. Jacob, G. Brodie, P.A. Schneider, Isotherms, kinetics and mechanism analysis of phosphorus recovery from aqueous solution by calcium-rich biochar produced from biosolids via microwave pyrolysis, J. Environ. Chem. Eng. 6 (2018) 395–403, https://doi.org/10.1016/j.jece.2017.12.011.

[2] Md.R. Awual, Efficient phosphate removal from water for controlling eutrophication using novel composite adsorbent, J. Clean. Prod. 228 (2019) 1311–1319, https://doi.org/10.1016/j.jclepro.2019.04.325.

[3] G. Chattopadhyaya, D.G. Macdonald, N.N. Bakhshi, J.S. Soltan Mohammadzadeh, A.K. Dalai, Preparation and characterization of chars and activated carbons from Saskatchewan lignite, Fuel Process. Technol. 87 (2006) 997–1006, https://doi.org/10.1016/j.fuproc.2006.07.004.

[4] J. Chen, H. Kong, D. Wu, X. Chen, D. Zhang, Z. Sun, Phosphate immobilization from aqueous solution by fly ashes in relation to their composition, J. Hazard. Mater. 139 (2007) 293–300, https://doi.org/10.1016/j.jhazmat.2006.06.034.

[5] S. Chen, Q. Yue, B. Gao, Q. Li, X. Xu, K. Fu, Adsorption of hexavalent chromium from aqueous solution by modified corn stalk: a fixed-bed column study, Bioresour. Technol., Spec. Issue Chall. Environ. Sci. Eng. 113 (2012) 114–120, https://doi.org/10.1016/j.biortech.2011.11.110.

[6] L. Dai, F. Tan, H. Li, N. Zhu, M. He, Q. Zhu, G. Hu, L. Wang, J. Zhao, Calcium-rich biochar from the pyrolysis of crab shell for phosphorus removal, J. Environ. Manag. 198 (2017) 70–74, https://doi.org/10.1016/j.jenvman.2017.04.057.

[7] W. Du, J. Sun, Y. Zan, Z. Zhang, J. Ji, M. Dou, F. Wang, Biomass-derived nitrogen-doped hierarchically porous carbon networks as efficient absorbents for phenol removal from wastewater over a wide pH range, RSC Adv. 7 (2017) 46629–46635, https://doi.org/10.1039/C7RA08374B.

[8] Y. Fu, Y. Shen, Z. Zhang, X. Ge, M. Chen, Activated bio-chars derived from rice husk via one- and two-step KOH-catalyzed pyrolysis for phenol adsorption, Sci. Total Environ. 646 (2019) 1567–1577, https://doi.org/10.1016/j.scitotenv.2018.07.423.

[9] R.P. Girón, R.R. Gil, I. Suárez-Ruiz, E. Fuente, B. Ruiz, Adsorbents/catalysts from forest biomass fly ash. Influence of alkaline activating agent, Microporous Mesoporous Mater., SI: Charact. Porous Solids X 209 (2015) 45–53, https://doi.org/10.1016/j.micromeso.2015.01.051.

[10] J.I. González Ocampo, D.M. Escobar Sierra, C.P. Ossa Orozco, Porous bodies of hydroxyapatite produced by a combination of the gel-casting and polymer sponge methods, J. Adv. Res. 7 (2016) 297–304, https://doi.org/10.1016/j.jare.2015.06.006.

[11] Q. He, P. Ruan, Z. Miao, K. Wan, M. Gao, X. Li, S. Huang, Adsorption of direct yellow brown D3G from aqueous solution using loaded modified low-cost lignite: performance and mechanism, Environ. Technol. 1–10 (2019), https://doi.org/10.1080/09593330.2019.1675774.

[12] G.W. Kajjumba, E. Yıldırım, S. Aydın, S. Emik, T. Ağun, F. Osra, J. Wasswa, A facile polymerisation of magnetic coal to enhanced phosphate removal from solution, J. Environ. Manag. 247 (2019) 356–362, https://doi.org/10.1016/j.jenvman.2019.06.088.

[13] M.A. Khan, Y.-T. Ahn, M. Kumar, W. Lee, B. Min, G. Kim, D.-W. Cho, W.B. Park, B.-H. Jeon, Adsorption studies for the removal of nitrate using modified lignite granular activated carbon, Sep. Sci. Technol. 46 (2011) 2575–2584, https://doi.org/10.1080/01496395.2011.601782.

[14] L. Kong, M. Han, K. Shih, M. Su, Z. Diao, J. Long, D. Chen, L. Hou, Y. Peng, Nano-rod Ca-decorated sludge derived carbon for removal of phosphorus, Environ. Pollut. 233 (2018) 698–705, https://doi.org/10.1016/j.envpol.2017.10.099.

[15] P.S. Kumar, L. Korving, M.C.M. van Loosdrecht, G.-J. Witkamp, Adsorption as a technology to achieve ultra-low concentrations of phosphate: research gaps and economic analysis, Water Res. X 4 (2019), 100029, https://doi.org/10.1016/j.wroa.2019.100029.

[16] J. Li, B. Li, H. Huang, X. Lv, N. Zhao, G. Guo, D. Zhang, Removal of phosphate from aqueous solution by dolomite-modified biochar derived from urban dewatered sewage sludge, Sci. Total Environ. 687 (2019) 460–469, https://doi.org/10.1016/j.scitotenv.2019.05.400.

[17] M. Li, C. Liu, H. Cao, H. Zhao, Y. Zhang, Z. Fan, KOH self-templating synthesis of three-dimensional hierarchical porous carbon materials for high performance supercapacitors, J. Mater. Chem. A 2 (2014) 14844–14851, https://doi.org/10.1039/C4TA02167C.

[18] J. Lin, S. He, X. Wang, H. Zhang, Y. Zhan, Removal of phosphate from aqueous solution by a novel Mg(OH)2/ZrO2 composite: adsorption behavior and mechanism, Colloids Surf. Physicochem. Eng. Asp. 561 (2019) 301–314, https://doi.org/10.1016/j.colsurfa.2018.11.001.

[19] W.-J. Liu, H. Jiang, H.-Q. Yu, Development of biochar-based functional materials: toward a sustainable platform carbon material, Chem. Rev. 115 (2015) 12251–12285, https://doi.org/10.1021/acs.chemrev.5b00195.

[20] J. Lladó, M. Solé-Sardans, C. Lao-Luque, E. Fuente, B. Ruiz, Removal of pharmaceutical industry pollutants by coal-based activated carbons, Process Saf. Environ. Prot. 104 (2016) 294–303, https://doi.org/10.1016/j.psep.2016.09.009.

[21] D. Lozano-Calero, P. Martìn-Palomeque, S. Madueño-Loriguillo, Determination of phosphorus in cola drinks, J. Chem. Educ. 73 (1996) 1173, https://doi.org/10.1021/ed073p1173.

[22] D. Lozano-Castelló, J.M. Calo, D. Cazorla-Amorós, A. Linares-Solano, Carbon activation with KOH as explored by temperature programmed techniques, and the effects of hydrogen, Carbon 45 (2007) 2529–2536, https://doi.org/10.1016/j.carbon.2007.08.021.

[23] J.P. Maity, T.-J. Lin, H.P.-H. Cheng, C.-Y. Chen, A.S. Reddy, S.B. Atla, Y.-F. Chang, H.-R. Chen, C.-C. Chen, Synthesis of brushite particles in reverse microemulsions of the biosurfactant surfactin, Int. J. Mol. Sci. 12 (2011) 3821–3830, https://doi.org/10.3390/ijms12063821.

[24] J.A. Marshall, B.J. Morton, R. Muhlack, D. Chittleborough, C.W. Kwong, Recovery of phosphate from calcium-containing aqueous solution resulting from biochar-induced calcium phosphate precipitation, J. Clean. Prod. 165 (2017) 27–35, https://doi.org/10.1016/j.jclepro.2017.07.042.

[25] D.T. Mekonnen, E. Alemayehu, B. Lennartz, Removal of phosphate ions from aqueous solutions by adsorption onto leftover coal, Water 12 (2020) 1381, https://doi.org/10.3390/w12051381.

[26] D. Mitrogiannis, M. Psychoyou, I. Baziotis, V.J. Inglezakis, N. Koukouzas, N. Tsoukalas, D. Palles, E. Kamitsos, G. Oikonomou, G. Markou, Removal of phosphate from aqueous solutions by adsorption onto Ca(OH)2 treated natural clinoptilolite, Chem. Eng. J. 320 (2017) 510–522, https://doi.org/10.1016/j.cej.2017.03.063.

[27] H. Nam, S. Wang, H.-R. Jeong, TMA and H2S gas removals using metal loaded on rice husk activated carbon for indoor air purification, Fuel 213 (2018) 186–194, https://doi.org/10.1016/j.fuel.2017.10.089.

[28] S. Ni, J. Chang, L. Chou, A novel bioactive porous CaSiO3 scaffold for bone tissue engineering, J. Biomed. Mater. Res. A 76A (2006) 196–205, https://doi.org/10.1002/jbm.a.30525.

[29] T. Otowa, R. Tanibata, M. Itoh, Production and adsorption characteristics of MAXSORB: High-surface-area active carbon, Gas. Sep. Purif. 7 (1993) 241–245, https://doi.org/10.1016/0950-4214(93)80024-Q.

[30] A. Panagopoulos, K.-J. Haralambous, Minimal Liquid Discharge (MLD) and Zero Liquid Discharge (ZLD) strategies for wastewater management and resource recovery – analysis, challenges and prospects, J. Environ. Chem. Eng. 8 (2020), 104418, https://doi.org/10.1016/j.jece.2020.104418.

[31] W. Parawira, I. Kudita, M.G. Nyandoroh, R. Zvauya, A study of industrial anaerobic treatment of opaque beer brewery wastewater in a tropical climate using a full-scale UASB reactor seeded with activated sludge, Process Biochem. 40 (2005) 593–599, https://doi.org/10.1016/j.procbio.2004.01.036.

[32] P.R. Prezas, B.M.G. Melo, L.C. Costa, M.A. Valente, M.C. Lança, J.M.G. Ventura, L. F.V. Pinto, M.P.F. Graça, TSDC and impedance spectroscopy measurements on hydroxyapatite, β-tricalcium phosphate and hydroxyapatite/β-tricalcium phosphate biphasic bioceramics, Appl. Surf. Sci., 7th International Conference on Advanced Nanomaterials, 2nd International Conference on Graphene Technology, 1st International Conference on Spintronics Materials 424, 2017: 28–38. ⟨https://doi.org/10.1016/j.apsusc.2017.02.225⟩.

[33] Y. Qi, A.F.A. Hoadley, A.L. Chaffee, G. Garnier, Characterisation of lignite as an industrial adsorbent, Fuel 90 (2011) 1567–1574, https://doi.org/10.1016/j.fuel.2011.01.015.

[34] V. Romanovski, Agricultural waste based-nanomaterials: green technology for water purification, in: K.A. Abd-Elsalam, M. Zahid (Eds.), Aquananotechnology, Micro and Nano Technologies, Elsevier, 2021, pp. 577–595, https://doi.org/10.1016/B978-0-12-821141-0.00013-6.

[35] H. Samaraweera, A. Sharp, J. Edwards, C.U. Pittman, X. Zhang, E.B. Hassan, R.V.K. G. Thirumalai, S. Warren, C. Reid, T. Mlsna, Lignite, thermally-modified and Ca/Mg-modified lignite for phosphate remediation, Sci. Total Environ. 773 (2021), 145631, https://doi.org/10.1016/j.scitotenv.2021.145631.

[36] R. Sharma, A. Sarswat, U. Pittman, D. C., Mohan, Cadmium and lead remediation using magnetic and non-magnetic sustainable biosorbents derived from Bauhinia purpurea pods, RSC Adv. 7 (2017) 8606–8624, https://doi.org/10.1039/C6RA25295H.

[37] S.K. Sriramoju, P.S. Dash, S. Majumdar, Meso-porous activated carbon from lignite waste and its application in methylene Blue adsorption and coke plant effluent treatment, J. Environ. Chem. Eng. 9 (2021), 104784, https://doi.org/10.1016/j.jece.2020.104784.

[38] E.A. Stefaniak, A. Buczynska, V. Novakovic, R. Kuduk, R.V. Grieken, Determination of chemical composition of individual airborne particles by SEM/EDX and micro-Raman spectrometry: a review, J. Phys.: Conf. Ser. 162 (2009), 012019, https://doi.org/10.1088/1742-6596/162/1/012019.

[39] C.A. Takaya, L.A. Fletcher, S. Singh, U.C. Okwuosa, A.B. Ross, Recovery of phosphate with chemically modified biochars, J. Environ. Chem. Eng. 4 (2016) 1156–1165, https://doi.org/10.1016/j.jece.2016.01.011.

[40] Y. Tang, X. Wang, Y. Yang, B. Gao, Y. Wan, Y.C. Li, D. Cheng, Activated-lignite-based super large granular slow-release fertilizers improve apple tree growth: synthesis, characterizations, and laboratory and field evaluations, J. Agric. Food Chem. 65 (2017) 5879–5889, https://doi.org/10.1021/acs.jafc.7b01699.

[41] USEPA, Nutrient Criteria Technical Guidance Manuals [WWW Document]. USEPA, 2018. URL ⟨https://www.epa.gov/nutrient-policy-data/nutrient-criteria-technical-guidance-manuals⟩ (accessed 12 April 2020).

[42] Z. Wang, S. Bakshi, C. Li, S.J. Parikh, H.-S. Hsieh, J.J. Pignatello, Modification of pyrogenic carbons for phosphate sorption through binding of a cationic polymer, J. Colloid Interface Sci. 579 (2020) 258–268, https://doi.org/10.1016/j.jcis.2020.06.054.

[43] H. Wei, S. Deng, B. Hu, Z. Chen, B. Wang, J. Huang, G. Yu, Granular bamboo-derived activated carbon for high CO(2) adsorption: the dominant role of narrow micropores, ChemSusChem 5 (2012) 2354–2360, https://doi.org/10.1002/cssc.201200570.

[44] E.D. Woumfo, J.M. Siéwé, D. Njopwouo, A fixed-bed column for phosphate removal from aqueous solutions using an andosol-bagasse mixture, J. Environ. Manag. 151 (2015) 450–460, https://doi.org/10.1016/j.jenvman.2014.11.029.

[45] B. Wu, J. Wan, Y. Zhang, B. Pan, I.M.C. Lo, Selective phosphate removal from water and wastewater using sorption: process fundamentals and removal mechanisms, Environ. Sci. Technol. 54 (2020) 50–66, https://doi.org/10.1021/acs.est.9b05569.

[46] J. Wu, A. Zhang, G. Li, Y. Wei, S. He, Z. Lin, X. Shen, Q. Wang, Effect of different components of single superphosphate on organic matter degradation and maturity during pig manure composting, Sci. Total Environ. 646 (2019) 587–594, https://doi.org/10.1016/j.scitotenv.2018.07.336.

[47] L. Wu, C. Wei, S. Zhang, Y. Wang, Y. Kuzyakov, X. Ding, MgO-modified biochar increases phosphate retention and rice yields in saline-alkaline soil, J. Clean. Prod. 235 (2019) 901–909, https://doi.org/10.1016/j.jclepro.2019.07.043.

[48] F. Xie, F. Wu, G. Liu, Y. Mu, C. Feng, H. Wang, J.P. Giesy, Removal of phosphate from eutrophic lakes through adsorption by in situ formation of magnesium hydroxide from diatomite, Environ. Sci. Technol. 48 (2014) 582–590, https://doi.org/10.1021/es4037379.

[49] H. Yang, Y. Wang, J. Bender, S. Xu, Removal of arsenate and chromate by lanthanum-modified granular ceramic material: the critical role of coating temperature, Sci. Rep. 9 (2019) 1–12, https://doi.org/10.1038/s41598-019-44165-8.

[50] W. Yang, X. Shi, J. Wang, W. Chen, L. Zhang, W. Zhang, X. Zhang, J. Lu, Fabrication of a novel bifunctional nanocomposite with improved selectivity for simultaneous nitrate and phosphate removal from water, ACS Appl. Mater. Interfaces 11 (2019) 35277–35285, https://doi.org/10.1021/acsami.9b08826.

[51] Q. Yin, H. Ren, R. Wang, Z. Zhao, Evaluation of nitrate and phosphate adsorption on Al-modified biochar: influence of Al content, Sci. Total Environ. 631–632 (2018) 895–903, https://doi.org/10.1016/j.scitotenv.2018.03.091.

[52] S.-Y. Yoon, C.-G. Lee, J.-A. Park, J.-H. Kim, S.-B. Kim, S.-H. Lee, J.-W. Choi, Kinetic, equilibrium and thermodynamic studies for phosphate adsorption to magnetic iron oxide nanoparticles, Chem. Eng. J. 236 (2014) 341–347, https://doi.org/10.1016/j.cej.2013.09.053.

[53] Q. Zhang, Z. Zhang, J. Teng, H. Huang, Q. Peng, T. Jiao, L. Hou, B. Li, Highly efficient phosphate sequestration in aqueous solutions using nanomagnesium hydroxide modified polystyrene materials, Ind. Eng. Chem. Res. 54 (2015) 2940–2949, https://doi.org/10.1021/ie503943z.

[54] Y. Zhang, M.S. Akindolie, X. Tian, B. Wu, Q. Hu, Z. Jiang, L. Wang, Y. Tao, B. Cao, J. Qu, Enhanced phosphate scavenging with effective recovery by magnetic porous biochar supported La(OH)3: kinetics, isotherms, mechanisms and applications for water and real wastewater, Bioresour. Technol. 319 (2021) 124232, https://doi.org/10.1016/j.biortech.2020.124232.

[55] L. Zhao, N. Guanhua, W. Hui, S. Qian, W. Gang, J. Bingyou, Z. Chao, Molecular structure characterization of lignite treated with ionic liquid via FTIR and XRD spectroscopy, Fuel 272 (2020), 117705, https://doi.org/10.1016/j.fuel.2020.117705.

[56] Y. Zheng, A.R. Zimmerman, B. Gao, Comparative investigation of characteristics and phosphate removal by engineered biochars with different loadings of magnesium, aluminum, or iron, Sci. Total Environ. 747 (2020) 141277, https://doi.org/10.1016/j.scitotenv.2020.141277.

[57] C. Zhong, Y. Deng, W. Hu, J. Qiao, L. Zhang, J. Zhang, A review of electrolyte materials and compositions for electrochemical supercapacitors, Chem. Soc. Rev. 44 (2015) 7484–7539, https://doi.org/10.1039/C5CS00303B.

[58] Y. Zhu, X. Zhang, Y. Chen, Q. Xie, J. Lan, M. Qian, N. He, A comparative study on the dissolution and solubility of hydroxylapatite and fluorapatite at 25°C and 45°C, Chem. Geol. 268 (2009) 89–96, https://doi.org/10.1016/j.chemgeo.2009.07.014.

[59] P. Regmi, J.L. Garcia Moscoso, S. Kumar, X. CaO, J. Mao, G. Schafran, Removal of copper and cadmium from aqueous solution using switchgrass biochar produced via hydrothermal carbonization process, J. Environ. Manage. 109 (2012) 61–69, https://doi.org/10.1016/j.jenvman.2012.04.047.